INTERNATIONAL JOURNAL OF HYDROGEN ENERGY 48 (2023) 25031–25043

Available online at www.sciencedirect.com

ScienceDirect

journal homepage: www.elsevier.com/locate/he

Soft-templated NiO–CeO_2 mixed oxides for biogas upgrading by direct CO_2 methanation

Luciano Atzori [a], *M. Giorgia Cutrufello* [a,b], *Daniela Meloni* [a], *Fausto Secci* [a], *Carla Cannas* [a,b], *Elisabetta Rombi* [a,b,*]

[a] *Dipartimento di Scienze Chimiche e Geologiche, Università di Cagliari, Complesso Universitario di Monserrato, S.S. 554 Bivio Sestu, 09042 Monserrato (CA), Italy*

[b] *Consorzio Interuniversitario Nazionale per La Scienza e Tecnologia Dei Materiali (INSTM), Via Giuseppe Giusti 9, 50121 Firenze (FI), Italy*

HIGHLIGHTS

- A series of NiO–CeO_2 mixed oxides is synthesized by the soft-template procedure.
- All samples show high surface areas and strong interactions between NiO and CeO_2.
- Small Ni^0 crystallites (6–9 nm) are obtained upon reduction regardless of Ni content.
- Good catalytic performance is obtained in the direct upgrading of a model biogas.
- Depending on composition and temperature, different steps control the overall rate.

ARTICLE INFO

Article history:
Received 31 October 2022
Received in revised form
1 February 2023
Accepted 27 March 2023
Available online 21 April 2023

Keywords:
Biogas upgrading
CO_2 methanation
Ni-based catalysts
CeO_2 support

ABSTRACT

The catalytic performance in the direct CO_2 methanation of a model biogas is investigated on NiO–CeO_2 nanostructured mixed oxides synthesized by the soft-template procedure with different Ni/Ce molar ratios. The samples are thoroughly characterized by means of ICP-AES, XRD, TEM and HR-TEM, N_2 physisorption at −196 °C, and H_2-TPR. They result to be constituted of CeO_2 rounded nanocrystals and of polycrystalline needle-like NiO particles. After a H_2-treatment at 400 °C for 1 h, the surface basic properties and the metal surface area are also assessed using CO_2 adsorption microcalorimetry and H_2-pulse chemisorption measurements, respectively. At increasing Ni content the Ni^0 surface area increases, while the opposite occurs for the number of basic sites. Using a $CO_2/CH_4/H_2$ feed, at 11,000 cm^3 h^{-1} $g_{cat}{}^{-1}$, CO_2 conversions in the 83–89 mol% range and methane selectivities >99.5 mol% are reached at 275 °C and atmospheric pressure, highlighting the very good performances of the investigated catalysts.

© 2023 Hydrogen Energy Publications LLC. Published by Elsevier Ltd. All rights reserved.

* *Corresponding author*. Dipartimento di Scienze Chimiche e Geologiche, Università di Cagliari, Complesso Universitario di Monserrato, S.S. 554 bivio Sestu, 09042 Monserrato, CA, Italy.
E-mail address: rombi@unica.it (E. Rombi).

https://doi.org/10.1016/j.ijhydene.2023.03.420
0360-3199/© 2023 Hydrogen Energy Publications LLC. Published by Elsevier Ltd. All rights reserved.

Introduction

Presently, over 85% of the global energy needs are met by the use of fossil fuels [1], the combustion of which is responsible for about 80% of the worldwide CO_2 emissions [2], widely considered the main factor causing global warming and climate change. Furthermore, considering that conventional energy resources (*i.e.*, oil and gas reserves) are mainly located in politically unstable regions, securing energy supply is a crucial question. Hence, in order to address these critical issues, significant efforts are aimed at efficiently exploiting renewable energy sources such as geothermal, wind, solar, and biomass energy. In this contest, biogas, commonly produced by the anaerobic digestion of biodegradable waste and substrates, is widely regarded as one of the most promising sources of renewable energy [3]. Methane (ca. 40–75 vol%) and carbon dioxide (25–60 vol%) are the main components of biogas [4], which also contains N_2, O_2, H_2S, and other contaminants in amounts that depend on the different production plants. In 2018 biogas was consumed for almost two thirds in the production of electricity and heat, whereas only about 5% was purified to biomethane [5]. However, the interest towards biogas upgrading for producing high-quality (>90%) biomethane (also known as renewable natural gas or upgraded biogas) is rapidly growing; in fact, while being carbon-neutral, biomethane is not distinguishable from natural gas and can thus be transported and utilized alike. Biogas upgrading technologies (water or chemical scrubbing, pressure swing adsorption, membrane permeation, cryogenic technology, biochar adsorption, biological removal) that involve CO_2 separation without its subsequent recovery and reuse have been reviewed since 2011 [4,6–14]. However, converting the high amount of CO_2 into CH_4 by the use of renewable hydrogen through the Power-to-Gas (P2G) process would make biogas valorization more attractive. Power-to-Gas joins the power grid to the gas grid, transforming surplus electricity to synthetic methane, first producing H_2 *via* water electrolysis and then converting it to synthetic methane through CO_2 hydrogenation [15–17]. Hence, three steps have to be taken into account when considering the whole process of methane generation and utilization: (i) CO_2 removal from the biogas stream, (ii) methanation of the recovered CO_2 through the P2G process, and (iii) injection of the synthesized methane into the transmission and distribution networks. However, the direct methanation of CO_2 in the biogas stream would simplify the process, avoiding the use of expensive separation technologies. In recent years, the production of methane has been extensively studied, analyzing various aspects (including thermodynamic, technological, economical, and environmental ones) of the possible different scenarios: biogas upgrading with no CO_2 valorization [18–20] and CO_2 methanation by P2G process without or after its removal from biogas [21–31].

As demonstrated by the numerous comprehensive reviews appeared in the literature over the last decade [32–43], the conversion of CO_2 into methane has been widely investigated on noble (Ru, Rh, Pt, Pd) and non-noble (Ni, Co, Fe, W, Mo) metals supported on a large number of metal oxides (e.g., Al_2O_3, SiO_2, ZrO_2, CeO_2, CeO_2–ZrO_2, TiO_2) synthesized with different methods, also in the presence of promoters. Moreover, the current research about the effects of the feed composition on the performance of the CO_2 methanation catalysts has been very recently reviewed [44], with the aim of identifying which properties the catalysts must have to be efficiently used in the direct methanation of biogas from different sources. It appears that, in spite of the extensive literature available on the CO_2 hydrogenation into methane, only in very few works this reaction has been studied on Ni-based catalysts in the presence of CH_4 in the gaseous feed mixture [45–52]. Supported Ni-based catalysts have been mostly investigated in carbon oxides hydrogenation, due to the low cost, high activity, and high methane selectivity of nickel. Among the various oxide supports, the peculiar features of CeO_2, like oxygen storage capacity, abundant oxygen vacancies, reducibility, and strong metal-support interactions, make this material particularly promising for use in CO_2 catalysis [53].

Considering the scarce literature [48] on the use of Ni–Ce catalysts for biogas upgrading, in the present work the catalytic performance in the direct CO_2 methanation of a model biogas (CH_4 67 mol% and CO_2 33 mol%) was investigated on a series of Ni/CeO_2 catalysts obtained from nanostructured mixed oxides synthesized with different Ni/Ce molar ratios by the unconventional soft-template procedure [54]. Such preparation method has proved to be effective for obtaining high surface areas [55] and guaranteeing strong Ni-support interactions [56].

Several physico-chemical techniques, such as inductively coupled plasma atomic emission spectroscopy (ICP-AES), X-ray diffraction (XRD), conventional and high resolution (HR) transmission electron microscopy (TEM), N_2 physisorption at −196 °C, temperature-programmed reduction (TPR), were used to characterize their composition, structure, texture, and redox features. The supported nickel catalysts were obtained by *in situ* reduction of the synthesized mixed oxides. Their surface basic properties were characterized using adsorption microcalorimetry of CO_2. The metal surface area was also determined by means of H_2-pulse chemisorption measurements.

Experimental

Materials

Cetyl-trimethyl-ammonium bromide (CTAB, ≥98%), $Ni(NO_3)_2 \cdot 6H_2O$ (99.999%), $Ce(NO_3)_3 \cdot 6H_2O$ (99%), and NaOH (pellets, 97%) were supplied by Aldrich. Ethanol (96%) and HNO_3 (≥65%) were supplied by Fluka. HCl (37%) was provided by VWR Chemicals. H_2O_2 (35%) was supplied by Carlo Erba. The gaseous feed mixture with known concentration of the components was supplied by SAPIO.

Synthesis of catalysts

NiO–CeO_2 mixed oxides with Ni/Ce molar ratios in the range 0.5–4.0 mol/mol were synthesized through the soft-template method, using $Ce(NO_3)_3 \cdot 6H_2O$ and $Ni(NO_3)_2 \cdot 6H_2O$ as the cerium and nickel oxides precursors, cetyl-trimethyl-

ammonium bromide as the template, and NaOH as the precipitating agent. Suitable amounts of the nitrate precursors and the templating agent (CTAB/precursors = 0.62 mol/mol) were dissolved under stirring in 100 cm^3 of distilled water at ambient temperature. A solution of NaOH (0.17 M) was added dropwise after 30 min until reaching a final pH value of 13. After stirring of the mixture for 15 h and digestion at 90 °C for 3 h, the obtained solid was filtered and washed with hot water (70 °C) until completely eliminating the bromide species (indicated by the absence of AgBr precipitate in the filtrate by reaction of bromides with $AgNO_3$). Finally, the recovered solid was dried at 110 °C for 6 h and then calcined at 450 °C for 4 h.

Characterization of catalysts

Ni and Ce contents were determined by means of ICP-AES analyses, performed with a 5110 ICP-OES spectrophotometer (Agilent Technologies). Each sample was dissolved in a H_2O_2 (35%) − HNO_3 (≥65%) mixture (1:1 by volume) and stirred at 80 °C for 2 h; a HCl (37%) − HNO_3 (≥65%) mixture (3:1 by volume) was then added and after 16 h at RT the solution was finally diluted to the desired volume with Milli-Q water.

The structural features were assessed by XRD using a PANalyitical X'Pert PRO diffractometer with a Cu-Kα radiation, a secondary monochromator, and a X'celerator detector. The average crystallite sizes were estimated by the Scherrer equation taking into account the Warren correction [57].

Textural analyses were carried out with a Sorptomatic 1990 System (Fisons Instruments), by determining the nitrogen adsorption-desorption isotherms at −196 °C. Before analyses, samples were heated overnight under vacuum up to 250 °C (heating rate, 1 °C min^{-1}). Surface area values were calculated by the BET equation. The pore size distribution (PSD) profiles were determined by applying the BJH method to the isotherm desorption branch.

Transmission electron microscopy (TEM) images were obtained with a JEOL 1400 Plus, equipped with a EDX module for the elemental analysis. A JEOL JEM 2010 UHR microscope, equipped with a Gatan Imaging Filter (GIF) with a 15 eV window and a 794 slow scan CCD camera, was instead used to collect high resolution TEM (HRTEM) images. Finely ground samples were dispersed in n-octane using an ultrasonic bath. The suspension was then dropped on a copper grid covered with a carbon thin film for the observation.

The redox properties were studied by means of H_2-TPR, by using a TPD/R/O 1100 apparatus (ThermoQuest) equipped with a thermal conductivity detector (TCD). Prior to the experiments, the samples (typically 0.020 g) were pretreated in air (15 cm^3 min^{-1}) at 450 °C for 1 h and then cooled under nitrogen (15 cm^3 min^{-1}) to the initial analysis temperature. TPR profiles were recorded under flowing H_2 (5 vol% in N_2; flow rate, 30 cm^3 min^{-1}) while heating (20 °C min^{-1}) from 40 °C to 950 °C.

CO_2 adsorption microcalorimetric runs were performed using a Tian-Calvet heat-flow microcalorimeter (Setaram), connected to a volumetric vacuum line. Samples (0.100 g, 40–80 mesh), previously reduced under flowing pure H_2 (15 cm^3 min^{-1}) at 400 °C for 1 h, were thermally pretreated at 250 °C for 12 h under vacuum (5×10^{-3} Pa). Analyses were carried out at 80 °C by admitting successive doses of the probe gas. The equilibrium pressure relative to each adsorbed amount was measured by means of a differential pressure gauge (Datametrics) and the thermal effect was recorded. The run was stopped at a final equilibrium pressure of about 160 Pa.

H_2-pulse chemisorption measurements were carried out in a TPD/R/O 1100 apparatus (ThermoQuest). Before analyses, the samples (0.100 g) were reduced under H_2 flow (15 cm^3 min^{-1}) at 400 °C for 1 h. Then, Ar (20 cm^3 min^{-1}) was used for purging (1 h) and subsequently cooling to 50 °C. Pulses of H_2 (5 vol% in Ar) were then admitted into the reactor until the area of the peaks remained constant. From the amount of chemisorbed H_2 the specific metal surface area was calculated assuming a H/Ni stoichiometric factor equal to 1, after calibration of the TCD signal.

Catalytic tests

Methanation tests were carried out in a tubular ($\varphi_{int} = 0.8$ cm) quartz-glass fixed-bed microreactor, at atmospheric pressure, in a temperature range between 200 and 380 °C, and at a space velocity (*SV*) value of 72,000 cm^3 h^{-1} g_{cat}^{-1}. Each temperature was maintained for 2 h and then was increased to the next setpoint with a heating rate of 2 °C min^{-1}. A fluidized bed of silicon carbide, realized by means of a compressed air flow in an external jacket, allowed the reactor to keep isothermal conditions once the desired temperature has been reached. A K-type thermocouple was located in the thermostatic jacket using a suitable thermal sheath and connected to a temperature-programmer/controller to monitor the temperature. A second K-type thermocouple was positioned inside the reactor in contact with the catalytic bed to check the temperature (no differences between the setpoint and the detected temperature values were observed). On selected samples, the influence of space velocity was also investigated by performing catalytic tests at 275 °C in the *SV* range 11,000–430,000 cm^3 h^{-1} g_{cat}^{-1}. Each catalytic run was repeated twice to test the reproducibility of the data.

Prior to the reaction, the catalyst (0.050 g) was pretreated in N_2 (30 cm^3 min^{-1}) at 400 °C overnight, subsequently reduced under H_2 flow (15 cm^3 min^{-1}) at the same temperature for 1 h, and then cooled in He (30 cm^3 min^{-1}) to the desired reaction temperature. The reactant gas mixture was composed of CO_2 (12.9 mol%), CH_4 (25.9 mol%), H_2 (55.2 mol%) and N_2 (6.0 mol%, used as the internal standard). The $CO_2/CH_4/H_2$ molar ratios of 1/2/4 were chosen to simulate the composition of a model biogas (CH_4, 67 mol%; CO_2, 33 mol%) and to have the stoichiometric amount of hydrogen required for the methanation reaction ($H_2/CO_2 = 4$ mol/mol).

At each reaction temperature and/or space velocity, online gas chromatographic (GC) analyses of the reactor effluent were performed after 1 h on stream (the time required to ensure steady state is reached), monitoring the catalytic performance during 2 h. An Agilent 6890 GC was used, equipped with a Carboxen 1010 PLOT capillary column and a TCD. Water was removed from the reaction mixture through an ice trap and a molecular sieves trap placed between the reactor outlet and the GC injection valve. The results of the quantitative analysis of the carbon-containing components were used for checking the carbon mass balance and for calculating CO_2 conversion (X_{CO_2}) and products selectivity (S_i)

through the following equations, where $\dot{n}_i$ are the molar flow rates.

$$X_{CO_2}\ (\text{mol\%}) = \frac{\left(\frac{\dot{n}_{CO_2}}{\dot{n}_{N_2}}\right)_{in} - \left(\frac{\dot{n}_{CO_2}}{\dot{n}_{N_2}}\right)_{out}}{\left(\frac{\dot{n}_{CO_2}}{\dot{n}_{N_2}}\right)_{in}} \cdot 100$$

$$S_{CH_4}\ (\text{mol\%}) = \frac{\left(\frac{\dot{n}_{CH_4}}{\dot{n}_{N_2}}\right)_{out} - \left(\frac{\dot{n}_{CH_4}}{\dot{n}_{N_2}}\right)_{in}}{\left(\frac{\dot{n}_{CO_2}}{\dot{n}_{N_2}}\right)_{in} - \left(\frac{\dot{n}_{CO_2}}{\dot{n}_{N_2}}\right)_{out}} \cdot 100$$

$$S_{CO}\ (\text{mol\%}) = \frac{\left(\frac{\dot{n}_{CO}}{\dot{n}_{N_2}}\right)_{out}}{\left(\frac{\dot{n}_{CO_2}}{\dot{n}_{N_2}}\right)_{in} - \left(\frac{\dot{n}_{CO_2}}{\dot{n}_{N_2}}\right)_{out}} \cdot 100$$

Results and discussion

Characterization of fresh samples

For all samples, the actual composition is in close agreement with the nominal one, as can be observed from the ICP-AES results reported in Table 1.

XRD patterns of the fresh materials (Fig. S1) exhibit the presence of reflections ascribable to NiO (PDF card: 044–1159) and cubic CeO_2 (PDF card: 034–0394). A mean crystallite size of 4.2 ± 0.5 nm and 7.6 ± 0.4 nm was obtained from NiO [200] and [220] reflections, respectively, strongly suggesting a preferential growth of the NiO particles along the [220] crystal planes. As for CeO_2, the crystallite size values calculated on the three reflections were similar to each other, the mean value being 3.0 ± 0.3 nm. The Ni/Ce molar ratio did not show any significant influence on the crystallite size of either NiO or CeO_2. These results are in agreement with those reported and discussed in a previous work for similar samples [56].

N_2 physisorption isotherms are reported in Fig. S2 and summarized in Table 1. According to the classification reported in Ref. [58], all isotherms can be classified as type IVa, with the presence of a hysteresis loop, typical of mesoporous solids. All the samples are characterized by high surface areas (S_{BET}), in the range 188–206 $m^2\ g^{-1}$. Both S_{BET} and the pore volume (V_p) slightly increase along with the nickel content. From the PSD profiles (Fig. S2, insets) it appears that the mean pore diameter (d_p) shifts to higher values (from ca. 5 to ca. 8 nm) at increasing Ni amounts.

Table 1 – Chemical composition and textural features of the fresh xNiCe samples.

Sample	Ni/Ce[a] (mol/mol)	Ni content[a] (wt%)	S_{BET}[b] ($m^2\ g^{-1}$)	V_p[b] ($cm^3\ g^{-1}$)
0.5NiCe	0.46	10.7	188	0.24
0.75NiCe	0.72	15.2	190	0.28
1.0NiCe	1.16	23.6	197	0.31
1.5NiCe	1.51	26.7	202	0.35
2.0NiCe	1.94	31.0	197	0.36
3.0NiCe	2.96	37.3	206	0.37
4.0NiCe	3.95	40.8	205	0.39

[a] Determined by ICP-AES.
[b] Determined by N_2 physisorption data.

Transmission electron microscopy characterization was performed on selected samples (0.75NiCe, 3.0NiCe, and 4.0NiCe); 3.0NiCe was also characterized with HR-TEM. Elemental mapping analysis was performed on 0.75NiCe and 3.0NiCe to assess the homogeneity of the mutual dispersion of the two oxides. For all the investigated catalysts, TEM imaging shows large aggregates of small, rounded nanoparticles, with an inter-particle worm-like porosity, as well as the presence of needle-like particles (Fig. 1). Whereas the rounded particles are constituted of CeO_2, the needle-like particles are presumably made up of NiO, as suggested by the increase in their amount with increasing Ni content (0.75NiCe <3.0NiCe <4.0NiCe) and in agreement with the preferential growth highlighted by XRD data. From the particle size distribution of the CeO_2 nanoparticles a mean diameter of 4.1 ± 0.8, 2.9 ± 0.5 nm, and 3.3 ± 0.8 nm has been calculated for 0.75NiCe, 3.0NiCe, and 4.0NiCe, respectively (Fig. S3). The particle size distribution of the NiO elongated particles, determined on the 3.0NiCe sample (Fig. S4), shows a mean value of 3.7 ± 0.8 nm, following a lognormal distribution, for the shorter dimension and a size range between 30 and 70 nm for the longer one. Despite the intrinsic limits of this type of analysis, related to the high degree of aggregation among the nanoparticles, their small size, and their irregular edges, these data are in good agreement with the size obtained from XRD measurements for the CeO_2 crystallites and for the shorter dimension of the NiO crystallites, suggesting a high crystallinity. As for NiO nanocrystals, their elongated shape confirms the preferential growth along the [220] plane revealed by XRD analysis, which showed the smaller width of the [220] peak located at a 2θ value of 62.6° (see Fig. S1). The great difference between the longer dimension value of the NiO particles obtained by TEM imaging (30–70 nm) and that obtained from the [220] XRD reflection (7.6 ± 0.4 nm) indicates a polycrystalline nature of the NiO nanoparticles. Combined with the corresponding bright-field TEM image (Fig. S5a), the dark-field one (Fig. S5b) points out the presence of both small round-like bright spots throughout the large aggregates and elongated bright spots, indicated by arrows, attributable to the crystalline nature of nanoparticles of the two phases, in agreement with XRD data.

HR-TEM imaging on 3.0NiCe (Fig. 2) allows observing the presence of the CeO_2 [111] crystal planes in the rounded particles constituting the large aggregates, confirming their crystalline nature; in the case of the needle-like particles, crystal planes were not observed, probably due to a shielding effect from the small CeO_2 nanoparticles. However, the Fast Fourier Transform (FFT) of the HR-TEM images allows highlighting the presence of spots corresponding to NiO [111] lattice planes.

Elemental chemical mapping of Ni, Ce, and O and their linear profile analysis on 0.75NiCe (Fig. S6) and 3.0NiCe (Fig. S7) confirms an overall homogeneous distribution of the three elements; this is a clear indication of the homogeneous dispersion of the two oxides into each other, which favors the interaction between the two phases.

The H_2-TPR profiles of all the catalysts (Fig. S8) show two main signals, the first in the range 150–380 °C and the second at higher temperatures (up to 750 °C), each one consisting of several overlapping contributions, which clearly indicates the presence of different reducible species. In agreement with

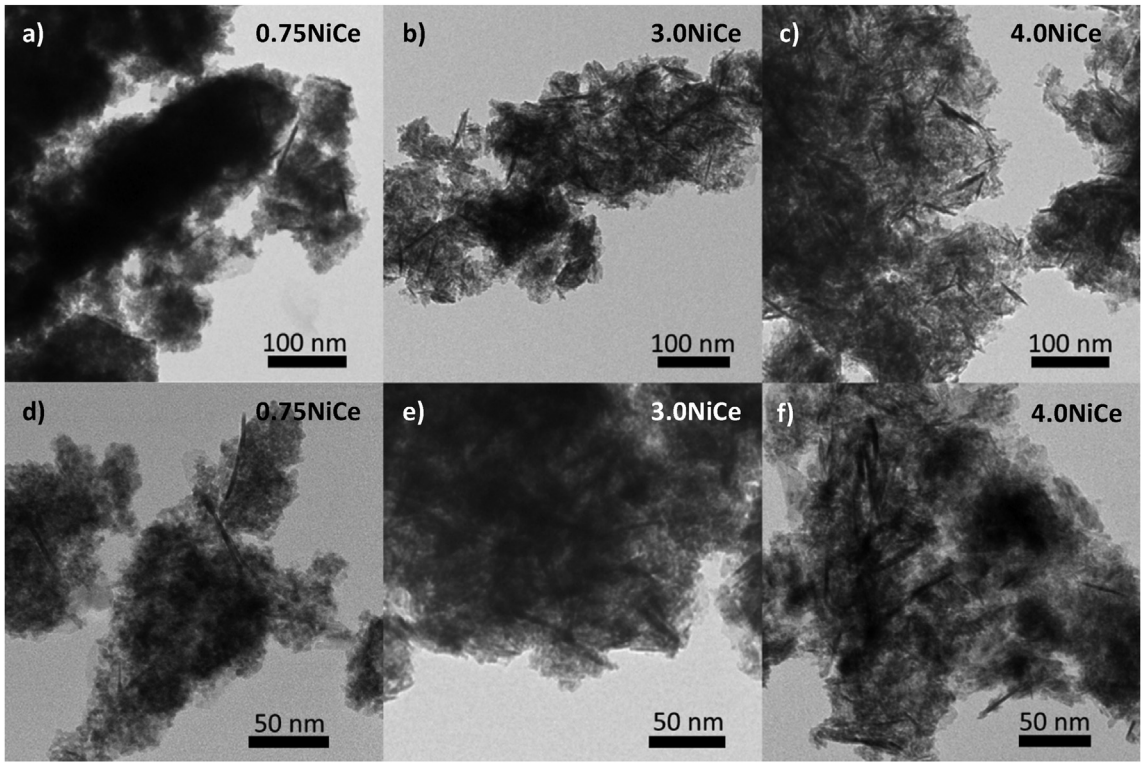

Fig. 1 – TEM images of 0.75NiCe (a,d), 3.0NiCe (b,e), and 4.0NiCe (c,f).

previously reported results [56,59], most of the hydrogen consumed in the high temperature region is ascribed to the reduction of nickel oxide, in the form of bulk-like particles dispersed on the ceria surface (β-peak) and of NiO species strongly interacting with CeO_2 (γ-peak) [60]. However, reduction of CeO_2 can be expected to some extent, as indicated by the high percentages (>100%) of H_2 consumed for completely reducing NiO, calculated according to the stoichiometry of the reaction $NiO + H_2 \rightarrow Ni^0 + H_2O$ (Table S1). Moreover, it should also be taken into account that, according to the literature [61], hydrogen-spillover processes from the Ni^0 particles to the oxide support could enhance the reducibility of ceria. Concerning the contribution at low temperature (α-peak), it can be related to the reduction of oxygen species adsorbed on defective sites where Ni and Ce species are in close interaction, located both at the NiO/CeO_2 interface or in the $NiO–CeO_2$ solid solution [62]. The presence of the α-peak in the TPR profiles of all the samples confirms the intimate contact between the two oxide components, as already suggested by the elemental chemical mapping. Moreover, the existence of Ni and Ce species in strong interaction in similar catalytic systems was already evidenced by Raman and X-ray photoelectron spectroscopies [63].

Characterization of reduced catalysts

CO_2 adsorption properties were studied on selected xNiCe catalysts by means of adsorption microcalorimetry. The

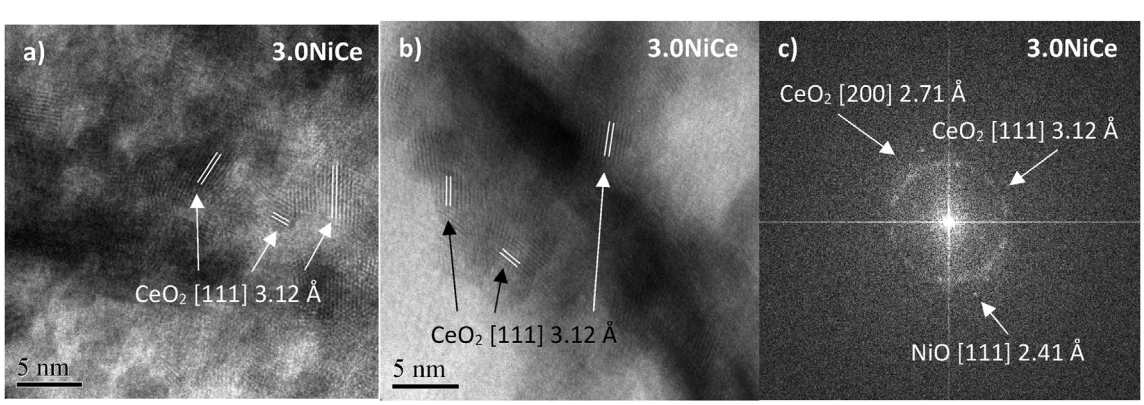

Fig. 2 – HR-TEM images (a,b) and FFT (c) of the 3.0NiCe sample.

microcalorimetric results, also compared to those of pure NiO and CeO_2, are reported in Fig. S9 and summarized in Table 2. The differential heat of adsorption (Q_{diff}) is plotted as a function of the CO_2 coverage (Fig. S9), allowing the assessment of basicity in terms of both concentration and strength distribution of the surface sites. In the evaluation of the basic character, only sites with a $Q_{diff} \geq 50$ kJ mol^{-1} were taken into account ($n_{B,tot}$, μmol g^{-1}), lower values being ascribed to nonspecific adsorption. Basic sites were roughly divided in weak ($n_{B,w}$, $50 \leq Q_{diff} < 90$ kJ mol^{-1}), medium-strength ($n_{B,m}$, $90 \leq Q_{diff} \leq 150$ kJ mol^{-1}), and strong ($n_{B,s}$, $Q_{diff} > 150$ kJ mol^{-1}) ones. The remarkably higher basicity of 0.5NiCe with respect to pure CeO_2 is mainly due to a manifest increase in the number of medium-strength and strong sites. An analogous trend was previously observed on a similar sample with a Ni/Ce molar ratio of 0.3 and was ascribed to the insertion of nickel in the ceria structure, which enhances the basic character of the NiCe catalysts through the increase in the number of oxygen vacancies [63]. However, the increase in Ni content also leads to the decrease in the number of basic sites responsible for CO_2 adsorption (Table 2).

The specific surface areas of the Ni^0 metal particles expressed per unit mass of catalyst, A_{met}, are reported in Table 3. Due to the presence of spillover phenomena, responsible for the transfer of atomic hydrogen from the metal to the ceria support [61], the values of the metal surface area and dispersion calculated by H_2 chemisorption techniques could be affected by a significant overestimation. However, although they cannot be considered as real data, the estimated A_{met} values can be confidently used to compare the ability of the xNiCe catalysts to adsorb and activate H_2. It can be observed (Fig. S10) that A_{met} linearly increases along with the nickel content, suggesting that not remarkable differences exist within the catalysts series in terms of metal dispersion.

Characterization of used samples

XRD patterns of the used catalysts are reported in Fig. S11. In the case of the 0.5NiCe catalyst, no reflections ascribable to any nickel phase are visible, while a reflection of very low intensity ascribable to the [111] planes of Ni^0 is observable in the case of 0.75NiCe (PDF Card 04–0850), suggesting that nickel oxide is almost completely reduced after the H_2-pretreatment at 400 °C and very highly dispersed Ni^0 nanocrystals are formed. The peaks of the Ni^0 phase become more and more intense with the increase in nickel content. However, only a limited increase (from ca. 5.7 to ca. 8.7 nm calculated from the [111] reflection) in the metal nanocrystals size is estimated for Ni/Ce ratios going from 1.0 to 4.0 mol/mol. This indicates that, irrespective of the catalyst composition, nickel retains a very good dispersion after the H_2-pretreatment and reaction, reasonably owing to very effective Ni-support interactions and also to a possible positive effect of a small amount of residual nickel oxide [64]. Indeed, the presence of peaks ascribable to the NiO phase for the catalysts with a Ni/Ce molar ratio ≥3.0 seems to indicate an incomplete nickel reduction after the H_2-pretreatment, although a partial reoxidation of the surface during the reaction and/or due to the exposure to air prior to XRD measurements cannot be excluded.

Table 2 – Microcalorimetric results for the xNiCe samples and the pure CeO_2 and NiO oxides after the H_2-pretreatment at 400 °C for 1 h.

Sample	$n_{B,w}$ μmol g^{-1}	$n_{B,m}$ μmol g^{-1}	$n_{B,s}$ μmol g^{-1}	$n_{B,tot}$ μmol g^{-1}
CeO_2	78	57	10	145
0.5NiCe	61	191	36	288
1.5NiCe	71	93	20	184
3.0NiCe	56	63	17	136
4.0NiCe[a]	46	32	22	100
NiO[a]	5	14	–	19

[a] From Ref. [63].

Table 3 – H_2 chemisorbed amount and specific surface areas of the Ni^0 metal particles for the xNiCe catalysts after H_2-pretreatment at 400 °C.

Sample	H_2 chemisorbed (μmol g_{cat}^{-1})	A_{met}[a] ($m^2_{Ni^0}$ g_{cat}^{-1})
0.5NiCe	90	7.0
0.75NiCe	117	9.2
1.0NiCe	156	12.2
1.5NiCe	203	15.9
2.0NiCe	235	18.4
3.0NiCe	247	19.3
4.0NiCe	277	21.7

[a] Automatically computed by the instrument software from the H_2 chemisorbed amount assuming a H/Ni stoichiometric factor equal to 1.

TEM imaging performed on 0.75NiCe (Fig. S12) and 3.0NiCe (Fig. S13) after use shows that the morphology of the large aggregates of spheroidal particles does not undergo any significant change. However, it is observed that the needle-like NiO particles disappear, indicating a major transformation of NiO into Ni^0, in agreement with XRD analysis. The absence of elongated crystalline NiO particles is also confirmed by dark-field TEM imaging of the used 0.75NiCe (Fig. S12b).

As in the case of the fresh sample, HR-TEM imaging of the 3.0NiCe catalyst after the methanation test only shows the crystal planes associated with CeO_2 (Fig. 3a and b). However, the existence of both Ni and NiO is evidenced by the presence of the corresponding [111] planes in the FFT image (Fig. 3c).

Catalytic results

Besides CO_2 hydrogenation, the reverse water gas shift (RWGS) reaction might also occur, being favored at higher temperatures because of its endothermicity. Moreover,

$$CO_2 + 4\,H_2 \rightleftarrows CH_4 + 2\,H_2O \quad \Delta H_{298}^0 = -165.0 \text{ kJ mol}^{-1} \quad (1)$$

$$CO_2 + H_2 \rightleftarrows CO + H_2O \quad \Delta H_{298}^0 = 41.2 \text{ kJ mol}^{-1} \quad (2)$$

$$CO + 3\,H_2 \rightleftarrows CH_4 + H_2O \quad \Delta H_{298}^0 = -206.1 \text{ kJ mol}^{-1} \quad (3)$$

Scheme 1 – Stoichiometric equations for: (1) CO_2 hydrogenation to methane; (2) reverse water gas shift; (3) CO hydrogenation to methane.

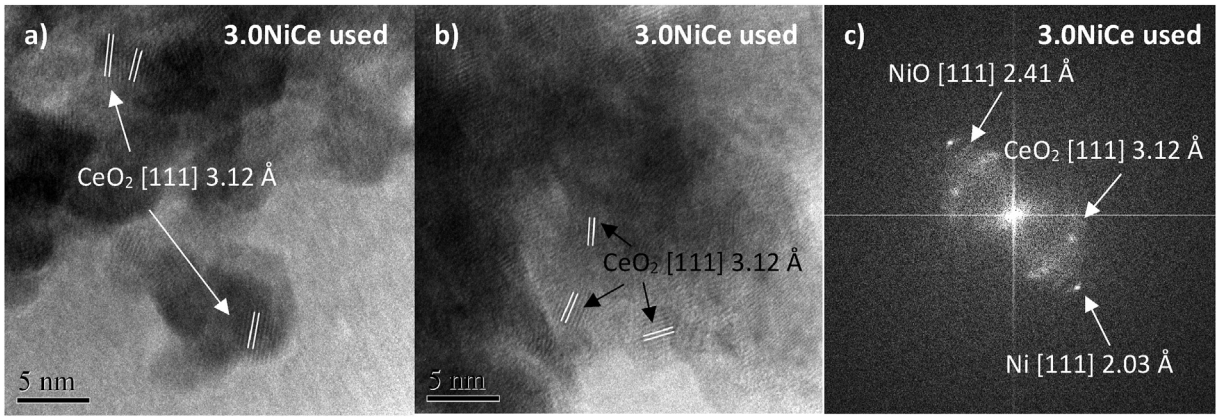

Fig. 3 – HR-TEM images (a,b) and FFT (c) of 3.0NiCe after the catalytic test.

methane formation through hydrogenation of the resulting CO is also possible (Scheme 1).

Unlike RWGS (Eq. (2)), the equilibrium conversion of CO_2 in the hydrogenation to methane (Eq. (1)) decreases with temperature, due to the exothermic character of the methanation reaction. In the presence of methane in the feed, the equilibrium conversion of CO_2, calculated by means of the total Gibbs free energy minimization method, was found to decrease from ca. 98 mol% to ca. 83 mol% in the range 200–380 °C [48]. Interestingly, such values turned out to be only slightly lower than those calculated through the same theoretical approach in the absence of methane [48,65], indicating that the presence of even high contents of this component has only a little effect on the CO_2 equilibrium conversion.

At 300 °C, the catalytic performances of 1.0NiCe, 2.0NiCe, and 4.0NiCe were found to be stable within 6 h on stream (Fig. S14). Pure CeO_2 tested in the same conditions showed a very low activity (X_{CO_2} < 5 mol%), therefore it was not further investigated. The values of CO_2 conversion (X_{CO_2}) as a function of temperature are shown for all the xNiCe catalysts in Fig. 4, where the equilibrium conversion is also reported for reference. For each reaction temperature, CO_2 conversions are reported as an average of the values determined throughout 2 h. CO_2 conversion is found to increase with temperature and appears to be lower than the equilibrium value at all the investigated temperatures (Fig. 4a). However, the fact that X_{CO_2} at 380 °C is practically the same (80 mol%) for all the catalysts, regardless of their composition, seems to indicate the achievement of equilibrium conditions, although the experimental conversion value is slightly lower than the theoretical one (83 mol%). Since deactivation phenomena were never observed, possible reactions leading to carbon formation (i.e., methane decomposition or CO disproportionation [48]) can be ruled out. Except for low amounts of carbon monoxide, methane was practically the only reaction product, with selectivity values > 99 mol% for all the catalysts up to 350 °C (Fig. 4b). The small decrease in S_{CH_4} observed at 380 °C can be ascribed to a slightly higher contribution of the RWGS reaction.

In Fig. 5, CO_2 conversions are reported as a function of the specific metal surface area. Interestingly, different trends can be observed depending on the reaction temperature. At 200 °C, X_{CO_2} slightly increases from ca. 12 to a constant value of ca. 16 mol% for A_{met} above 10 $m^2_{Ni^0}\ g_{cat}^{-1}$. A continuous increase in conversion from ca. 20 to ca. 40 mol% and from ca. 38 to ca. 70 mol% is instead observed at 225 and 250 °C, respectively, over the whole investigated range of A_{met}. At 275 °C, the conversion increases up to an A_{met} value of ca. 18 $m^2_{Ni^0}\ g_{cat}^{-1}$ (corresponding to the 2.0NiCe sample) and then stands at 77 mol%. It is noteworthy that the increase in X_{CO_2} is particularly marked between the two catalysts 0.5NiCe (54 mol%) and 0.75NiCe (71 mol%). A further increase in the reaction temperature makes progressively narrower the A_{met} range (and therefore the Ni/Ce molar ratio range) within which X_{CO_2} grows, until a constant value of ca. 80 mol% is achieved at 380 °C for all the catalysts.

The observed trends of X_{CO_2} as a function of the specific metal surface area strongly suggest that the concentration of the Ni^0 sites is not the only parameter which affects the catalytic activity. In agreement with Aldana et al. [66], in previous papers dealing with CO_2 methanation [56] and CO + CO_2 co-methanation [63] on similar soft-templated NiCe catalysts, a reaction pathway was proposed where H_2 is dissociatively adsorbed and activated on Ni^0 sites (formation of H_{ads} species) while CO_2 is mainly activated on the basic sites of ceria, on which it is adsorbed in the form of hydrogen carbonates and carbonates (mono-, bi-, and poly-dentate). Then, the H_{ads} species migrate from the metal sites through spillover processes [61,67] towards the ceria sites, where methane is formed through the consecutive hydrogenation of the oxygenated intermediates (formates, formaldehyde-type and methoxy species) and finally released to the gaseous phase. It is important to take into account that reaction temperature reasonably affects the rate of each of the steps involved in the catalytic process to a different extent. Anyway, it can be easily guessed that the simultaneous presence of Ni^0 and basic surface sites in close interaction is crucial to achieve a good catalytic performance, as also proposed by other authors [68].

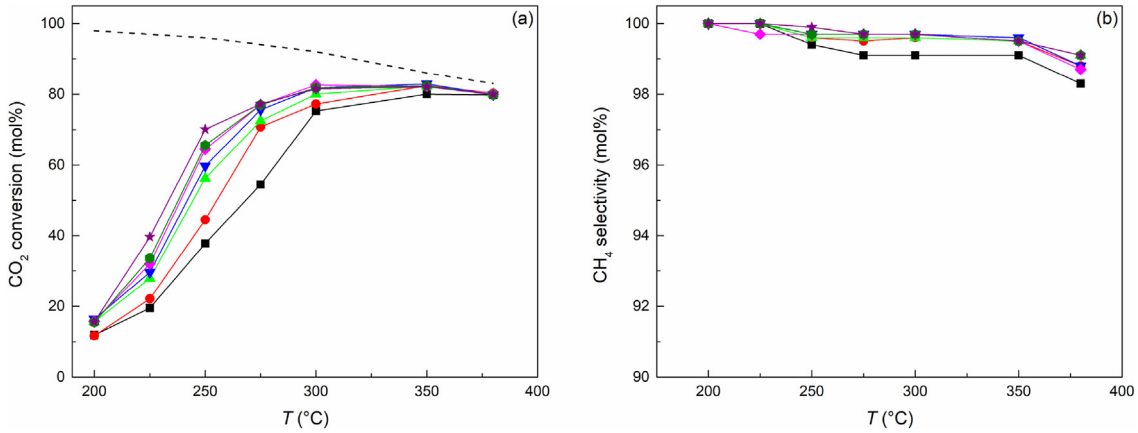

Fig. 4 – CO_2 conversion (a) and CH_4 selectivity (b) as a function of reaction temperature: (■), 0.5NiCe; (●), 0.75NiCe; (▲), 1.0NiCe; (▼), 1.5NiCe; (◆), 2.0NiCe; (●), 3.0NiCe; (★), 4.0NiCe. Other reaction conditions: m_{cat} = 0.050 g, $CO_2/CH_4/H_2$ molar ratios = 1/2/4, SV = 72,000 $cm^3\ h^{-1}\ g_{cat}^{-1}$. Dashed line represents the equilibrium conversion.

At the lowest investigated temperature (200 °C) more steps are most likely kinetically limited, leading to a low conversion regardless of the catalysts composition. By converse, at the highest temperature (380 °C) all the steps are sufficiently fast to achieve equilibrium whatever the catalyst. The progressive increase in CO_2 conversion along with the specific Ni^0 surface area observed at 225 and 250 °C seems to indicate that the catalytic activity is mainly governed by the ability of the catalyst to chemisorb and activate H_2. The much less important influence of CO_2 activation is confirmed by the observation that the capacity to adsorb CO_2 decreases passing from 0.5NiCe to 4.0NiCe (Table 2). In the range 275–350 °C, CO_2 conversion as a function of A_{met} initially increases, confirming the major role of H_2 activation in determining the overall rate of the catalytic process. Then it reaches an almost constant value, starting from different A_{met} values depending on the temperatures. Apparently, from that A_{met} value onwards, the further increase in the number of sites capable of activating hydrogen is no longer beneficial. This indicates that the rate of the whole process is governed by other steps.

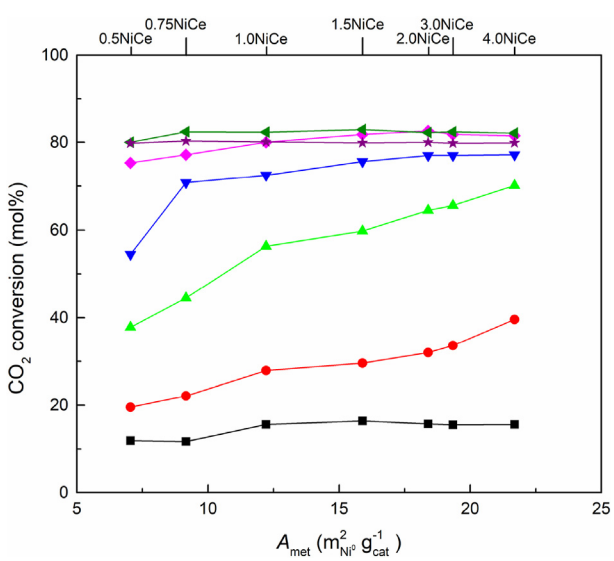

Fig. 5 – CO_2 conversion as a function of the specific metal surface area at the different investigated temperatures: (■), 200 °C; (●), 225 °C; (▲), 250 °C; (▼), 275 °C; (◆), 300 °C; (◀), 350 °C; (★), 380 °C. Other reaction conditions: m_{cat} = 0.050 g, $CO_2/CH_4/H_2$ molar ratios = 1/2/4, SV = 72,000 $cm^3\ h^{-1}\ g_{cat}^{-1}$.

Catalytic tests in a wide range of space velocities (11,000–430,000 $cm^3\ h^{-1}\ g_{cat}^{-1}$) were performed at 275 °C on selected samples (Fig. 6). Once again, methane selectivity is always higher than 99 mol%. As expected, CO_2 conversion is found to decrease with the increase in SV. For 0.5NiCe, X_{CO_2} is always lower than that of the other catalysts. Nonetheless, at the lowest SV value its catalytic behavior approaches that of the others, which show practically the same conversion, very close to the equilibrium value.

Such results confirm that the factors that mostly influence CO_2 conversion change depending on the reaction conditions. At more kinetically unfavored reaction conditions (low temperature or high SV), CO_2 conversion seems to be governed by the ability of the catalyst to activate H_2, which increases along with the nickel content. On the contrary, under more favorable temperature and SV, the reaction is mainly influenced by the rate of some steps of the CO_2 methanation mechanism subsequent to the H_2 activation, that could limit the conversion irrespective to the catalyst composition.

In the few papers dealing with the upgrading of biogas by direct CO_2 methanation, the catalytic performance of samples of different nature and composition are studied in a wide range of reaction conditions, in terms of temperature, pressure, and space velocity. Therefore, a clear comparison of the results turns out to be challenging. Nevertheless, the performances of the present catalysts are compared in Table 4 with those reported in the literature for other Ni-based systems. The catalytic behavior of Ni-based catalysts supported on commercial γ-Al_2O_3 was reported for Ni contents of 20 [45,48]

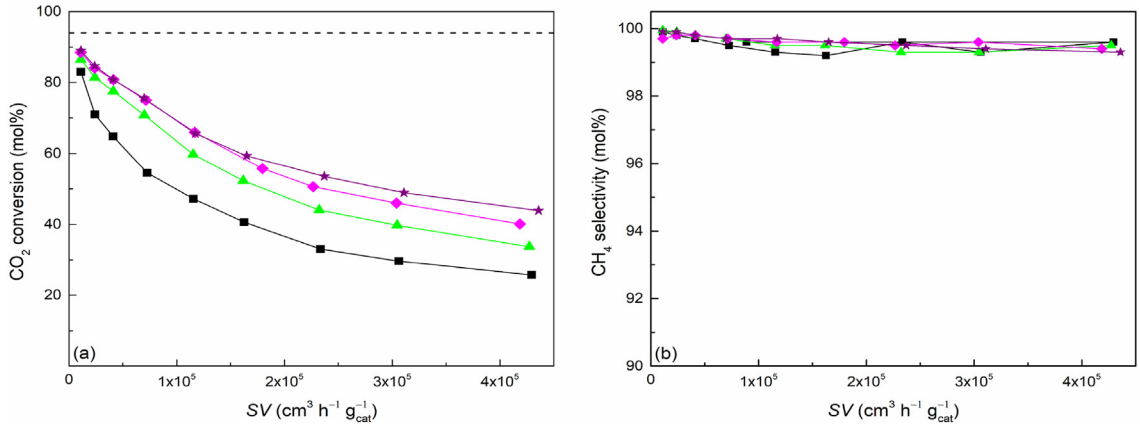

Fig. 6 – CO_2 conversion and CH_4 selectivity as a function of space velocity at 275 °C. (■), 0.5NiCe; (▲), 1.0NiCe; (◆), 2.0NiCe; (★), 4.0NiCe. Dashed line represents equilibrium conversion.

and 40 wt% [48], also in the presence of Ru as the promoter [45]. At 2 bar, 350 °C, 56,000 $cm^3\ g_{cat}^{-1}\ h^{-1}$, and $CO_2/H_2 = 1/4$ mol/mol, CO_2 conversion on the unpromoted catalyst did not exceed 72 mol% regardless of the CH_4/CO_2 molar ratio (1/1 or 2/1) in the feed, reaching the value of ca. 81 mol% only in the case of the 20Ni0·5Ru/Al_2O_3 sample. However, methane selectivity was always higher than 99 mol% [45]. At a lower *SV* value (30,000 $cm^3\ h^{-1}\ g_{cat}^{-1}$), a conversion of ca. 82 mol% was attained for Al_2O_3-supported catalysts with both 20 and 40 wt % of Ni [48], but with lower values of S_{CH_4} (ca. 80 mol%). Similar results were obtained using CeO_2 as the support in the Ni20–CeO_2 catalyst [48]. A Ni–Mg–Al catalyst (20 wt% of Ni) was tested at 400 °C, atmospheric pressure, and 30,000 $cm^3\ h^{-1}\ g_{cat}^{-1}$, varying the CH_4/CO_2 molar ratio from 0.67 to 1.9 [46]: in the presence of increasing amounts of methane in the gaseous mixture, X_{CO_2} decreased from 67 to 54 mol%, while S_{CH_4} remained constant at ca. 98 mol%. The effect of CH_4 content in the feed was also investigated on Ni(15 wt %)/CeO_2–ZrO_2 catalysts promoted with Co [47]: at 350 °C, atmospheric pressure, and 12,000 $cm^3\ h^{-1}\ g_{cat}^{-1}$, CO_2 conversion was found to increase from 72 to 78 mol% at increasing CH_4/CO_2 molar ratios (from 0.26 to 0.88 mol/mol); a very slight increase in S_{CH_4} from 97 to 99 mol% was also observed. In another study [49], Ni-based catalysts with a metal content of ca. 10 wt% were prepared by impregnation on porous silica (SP), silica fiber (SF), and a carbon nanotubes-silica fiber composite (CNT-SF). Performing the reaction at 10 bar, 350 °C, $CH_4/CO_2 = 1.6/1$ mol/mol, and $SV = 12{,}000\ cm^3\ h^{-1}\ g_{cat}^{-1}$, the best results were obtained on the Ni/CNT-SF catalyst, which showed X_{CO_2} and S_{CH_4} values of 86.3 mol% and 97.0 mol%, respectively. A further improvement of the catalytic performance (X_{CO_2} and S_{CH_4} values of 95 mol% and 98 mol%, respectively, at 24,000 $cm^3\ h^{-1}\ g_{cat}^{-1}$) was found for the Ni–2Mg/SF sample after doping with 2 wt% of Mg [49]. From the comparison of the results from the literature with the present ones (Table 4), some relevant aspects can be highlighted. Noteworthy, at the temperature of 350 °C, atmospheric pressure, and remarkably higher space velocity (72,000 $cm^3\ h^{-1}\ g_{cat}^{-1}$), all the prepared xNiCe catalysts are able to achieve CO_2 conversions ≥80 mol% and methane selectivity >99 mol%. Also, such X_{CO_2} and S_{CH_4} values can be reached by catalysts with Ni/Ce molar ratios ≥1.0 even at lower temperatures (300 °C) (Fig. 4). By considering the lowest *GHSV* (12,000 $cm^3\ h^{-1}\ g_{cat}^{-1}$) investigated in Refs. [47,49], it emerges that, at comparable values (11,000 $cm^3\ h^{-1}\ g_{cat}^{-1}$), the present catalysts allow CO_2 conversions in the 83–89 mol% range to be reached at 275 °C and atmospheric pressure, with selectivity to methane >99.5 mol% (Fig. 6). Though obtained under milder reaction conditions, less favorable from both the thermodynamic (atmospheric pressure) and kinetic (lower temperature) point of view, these results are considerably better than those reported for Ni–Co/Al_2O_3 catalysts at 350 °C [47] and comparable to those showed by the Ni/CNT-SF catalyst at 350 °C and 10 bar [49] (Table 4), proving that xNiCe are promising catalysts for biogas upgrading through direct CO_2 methanation.

An important aspect that should be taken into account when analyzing the performance of the catalysts to be used for biogas upgrading by the direct CO_2 methanation is related to the strict requirements usually imposed in terms of residual CO_2 and H_2 concentrations, which in turn depend on the speculated end-use of the upgraded biogas and also by the different national regulations. For instance, the residual CO_2 content in biomethane destined for gas grid injection has to be lower than 2.5 mol% in Italy [69] and 2 mol% in Switzerland [70]. As for hydrogen, the European standard EN 16726 (Annex E – "Hydrogen Admissible Concentrations in natural gas systems") [71] provides directives on the residual H_2 concentration, pointing out that the proper limits have to be evaluated case by case depending on the possible end-uses. The highest H_2 content generally considered is 2 mol% [20], however various studies have shown that up to 10 mol% of hydrogen can be added to most parts of natural gas systems with no adverse effects [72]. Indeed, Switzerland and Germany regulations indicate limits up to 6 and 10 mol%, respectively [70,73].

From this point of view, it appears that the 89 mol% of CO_2 conversion, obtained with both the 2.0NiCe and 4.0NiCe catalysts, corresponds to residual concentrations of ca. 2.6 mol% and 17 mol% for carbon dioxide and hydrogen, respectively. Such amounts, while resulting very close to the limits imposed for CO_2, are not yet satisfactory with regard to hydrogen. However, considering that the catalytic performance has been studied using a slight excess of hydrogen and

Table 4 – Comparison of the present catalytic results for biomethane upgrading by direct CO_2 methanation with those reported in the literature.

Catalyst	Ni (wt%)	H_2:CO_2 (mol/mol)	CH_4:CO_2 (mol/mol)	CH_4 in the feed (vol%)	P (bar)	T (°C)	m_{cat} (g)	SV ($cm^3\ h^{-1}\ g_{cat}^{-1}$)	X_{CO2} (mol%)	S_{CH_4} (mol%)	Ref.
$20Ni/Al_2O_3$	20.0	4:1	1:1	14.3	2	350	0.150	56,000	70.8	99.5	[45]
$20Ni/Al_2O_3$	20.0	4:1	2:1	28.6	2	350	0.150	56,000	70.6	99.4	[45]
$20Ni0{\cdot}5Ru/Al_2O_3$	20.0	4:1	2:1	28.6	2	350	0.150	56,000	ca. 81	ca. 100	[45]
Ni–Mg–Al	20.0	4:1	0.67:1	11.8	1	400	0.500	30,000	67	ca. 98	[46]
Ni–Mg–Al	20.0	4:1	1:1	16.7	1	400	0.500	30,000	64	ca. 98	[46]
Ni–Mg–Al	20.0	4:1	1.9:1	27.1	1	400	0.500	30,000	54	ca. 98	[46]
Ni–Co/CZ	15.7	4:1	0.26:1	5.0	1	350	0.250	12,000	72	97.0	[47]
Ni–Co/CZ	15.7	4:1	0.55:1	10.0	1	350	0.250	12,000	74	98.0	[47]
Ni–Co/CZ	15.7	4:1	0.88:1	15.0	1	350	0.250	12,000	78	99.0	[47]
$Ni20–CeO_2$	18.6	4:1	1:1	15.4	2	350	0.200	30,000	ca. 82	ca.78	[48]
$Ni20–Al_2O_3$	19.2	4:1	1:1	15.4	2	350	0.200	30,000	ca. 82	ca. 80	[48]
$Ni40–Al_2O_3$	36.9	4:1	1:1	15.4	2	350	0.200	30,000	ca. 82	ca. 80	[48]
Ni/CNT-SF	9.4	4:1	1.6:1	24.2	10	350	0.100	12,000	86.3	97.0	[49]
Ni/CNT-SF	9.4	4:1	1.6:1	24.2	10	350	0.100	36,000	77.9	>98	[49]
Ni–2Mg/SF	9.5	4:1	1.6:1	24.2	10	350	0.100	24,000	95.0	98.0	[49]
$10Ni/Al_2O_3$	10.3	4:1	2.3:1	–	1	350	0.500	30,000	57	>99.5	[52]
$7.5Ni\text{-}2.5Fe/Al_2O_3$	7.4	4:1	2.3:1	–	1	350	0.500	30,000	72	>99.5	[52]
0.5NiCe	10.7	4:1	2:1	25.9	1	350	0.050	72,000	80.0	99.5	[this work]
0.75NiCe	15.2	4:1	2:1	25.9	1	350	0.050	72,000	82.4	99.5	[this work]
1.0NiCe	23.6	4:1	2:1	25.9	1	350	0.050	72,000	82.3	99.5	[this work]
4.0NiCe	40.8	4:1	2:1	25.9	1	350	0.050	72,000	82.1	99.5	[this work]

relatively mild reaction conditions (atmospheric pressure and 275 °C), it can be reasonably expected that by carrying out the reaction under more favorable conditions, especially in terms of pressure, the final concentration of both CO_2 and H_2 may decrease below the requirements established by current regulations. In addition, it is important to take into account that over the last decade a growing interest has been devoted to the study and development of technological solutions that make possible the safe use of synthetic natural gas blended with hydrogen in concentration up to 30–50 mol%, which would allow important energy and environmental benefits [74–78].

Conclusions

A series of NiO–CeO_2 nanostructured mixed oxides with different Ni/Ce molar ratios (from 0.5 to 4.0 mol/mol) was synthesized with high surface areas (between 188 and 206 $m^2\ g^{-1}$) by the soft-template procedure. After a H_2-pretreatment at 400 °C for 1 h, the catalysts were used in the direct methanation of CO_2 contained in a model biogas. From XRD and TEM results, it was found that the samples were constituted of CeO_2 rounded nanocrystals (3–4 nm in size) and of polycrystalline elongated NiO particles with dimensions of ca. 4 nm × 30–70 nm. The close contact between the two oxides was evidenced by EDX results, which showed an overall homogeneous distribution of Ni, Ce, and O. The presence of strong interactions between NiO and CeO_2 was confirmed by the appearance of the α-peak in the H_2-TPR profiles of all the samples. CO_2 adsorption microcalorimetric tests performed on the catalysts after H_2 pretreatment at 400 °C for 1 h showed that the number of basic sites decreases with the increase in Ni content. By converse, the value of the Ni^0 surface area was found to increase with the same parameter, suggesting that the metal dispersion is comparable within the catalysts series. This is confirmed by XRD patterns of the catalysts after use, from which sizes of Ni^0 nanocrystals from ca. 5.7 to ca. 8.7 nm were calculated for Ni/Ce ratios in the range 1.0–4.0 mol/mol. CO_2 conversion was found to increase with temperature up to 350 °C, at which $X_{CO_2} \geq 80$ mol% and $S_{CH_4} > 99$ mol% were obtained regardless of the catalyst composition. The trend of X_{CO_2} as a function of Ni content, to which the number of sites responsible for either H_2 or CO_2 activation is related, was different depending on the reaction temperature. This indicates that the ability of the catalyst to activate H_2 is not the only parameter which affects the catalytic activity; indeed, at favorable temperature and SV, other steps would control the overall reaction rate. The performance of the present catalysts was found to be comparable – if not better – than that reported in the literature for other Ni-based catalysts. Given that a very good methanation activity was obtained even at mild reaction conditions, a remarkable enhancement is expected by a further optimisation of the operating parameters, especially in terms of pressure.

Declaration of competing interest

The authors declare that they have no known competing financial interests or personal relationships that could have appeared to influence the work reported in this paper.

Acknowledgements

Financial contribution of Fondazione di Sardegna (FdS) grant number F72F20000240007(2019) – Surface-tailored Materials for Sustainable Environmental Applications – is gratefully

acknowledged. Thanks are due to dr. Andrea Ardu and to the "Centro Servizi di Ateneo per la Ricerca (CeSAR)" for the use of the TEM measurements performed with JEOL JEM 1400 PLUS and JEOL JEM 2010 URP equipped with the Gatan Image Filter.

Appendix A. Supplementary data

Supplementary data to this article can be found online at https://doi.org/10.1016/j.ijhydene.2023.03.420.

REFERENCES

[1] Rackley SA. Carbon capture and storage. 2nd ed. Oxford: Butterworth-Heinemann; 2017.
[2] Special report on global warming of 1.5 °C. April 2020. https://www.ipcc.ch/sr15/.
[3] Achinas S, Achinas V, Euverink GJW. A technological overview of biogas production from biowaste. Engineering 2017;3:299–307. https://doi.org/10.1016/J.ENG.2017.03.002.
[4] Ryckebosch E, Drouillon M, Vervaeren H. Techniques for transformation of biogas to biomethane. Biomass Bioenergy 2011;35:1633–45. https://doi.org/10.1016/j.biombioe.2011.02.033.
[5] International Energy Agency (IEA). Outlook for biogas and biomethane: prospects for organic growth. 2020. https://www.iea.org/reports/outlook-for-biogas-and-biomethane-prospects-for-organic-growth.
[6] Bauer F, Persson T, Hulteberg C, Tamm D. Biogas upgrading – Technology overview, comparison and perspectives for the future. Biofuels Bioprod Bioref 2013;7:499–511. https://doi.org/10.1002/bbb.1423.
[7] Sun Q, Li H, Yan J, Liu L, Yu Z, Yu X. Selection of appropriate biogas upgrading technology – A review of biogas cleaning, upgrading and utilisation. Renew Sustain Energy Rev 2015;51:521–32. https://doi.org/10.1016/j.rser.2015.06.029.
[8] Thiruselvi D, Kumar PS, Kumar MA, Lay C-H, Aathika S, Mani Y, Jagadiswary D, Dhanasekaran A, Shanmugam P, Sivanesan S, Show P-L. A critical Review on global trends in biogas scenario with its up-gradation techniques for fuel cell and future perspectives. Int J Hydrogen Energy 2021;46:16734–50. https://doi.org/10.1016/j.ijhydene.2020.10.023.
[9] Muntaha N, Rain MI, Goni LKMO, Shaikh MAA, Jamal MS, Hossain M. A review on carbon dioxide minimization in biogas upgradation technology by chemical absorption processes. ACS Omega 2022;7:33680–98. https://doi.org/10.1021/acsomega.2c03514.
[10] Bahrun MHV, Bono A, Othman N, Abbas M, Zaini A. Carbon dioxide removal from biogas through pressure swing adsorption – a review. Chem Eng Res Des 2022;183:285–306. https://doi.org/10.1016/j.cherd.2022.05.012.
[11] Bi Y, Ju Y. Review on cryogenic technologies for CO_2 removal from natural gas. Front Energy 2022;16:793–811. https://doi.org/10.1007/s11708-022-0821-0.
[12] Aghel B, Behaein S, Alobaid F. CO2 capture from biogas by biomass-based adsorbents: a review. Fuel 2022;328:125276. https://doi.org/10.1016/j.fuel.2022.125276.
[13] Wu L, Wei W, Song L, Wózniak-Karczewska M, Chrzanowski Ł, Ni B-J. Upgrading biogas produced in anaerobic digestion: biological removal and bioconversion of CO_2 in biogas. Renew Sustain Energy Rev 2021;150:111448. https://doi.org/10.1016/j.rser.2021.111448.
[14] Gkotsis P, Kougias K, Mitraka M, Zouboulis A. Biogas upgrading technologies – recent advances in membrane-based processes. Int J Hydrogen Energy 2023;48:3965–93. https://doi.org/10.1016/j.ijhydene.2022.10.228.
[15] Wulf C, Linßen J, Zapp P. Review of power-to-gas projects in europe. Energy Proc 2018;155:367–78. https://doi.org/10.1016/j.egypro.2018.11.041.
[16] Iaquaniello G, Setini S, Salladini A, De Falco M. CO_2 valorization through direct methanation of flue gas and renewable hydrogen: a technical and economic assessment. Int J Hydrogen Energy 2018;43:17069–81. https://doi.org/10.1016/j.ijhydene.2018.07.099.
[17] Thema M, Bauer F, Sterner M. Power-to-gas: electrolysis and methanation status review. Renew Sustain Energy Rev 2019;112:775–87. https://doi.org/10.1016/j.rser.2019.06.030.
[18] Yousef AM, El-Maghlany WM, Eldrainy YA, Attia A. Upgrading biogas to biomethane and liquid CO_2: a novel cryogenic process. Fuel 2019;251:611–28. https://doi.org/10.1016/j.fuel.2019.03.127.
[19] Lombardi L, Francini G. Techno-economic and environmental assessment of the main biogas upgrading technologies. Renew Energy 2020;156:440–58. https://doi.org/10.1016/j.renene.2020.04.083.
[20] Barelli I, Bidini G, Ottaviano PA, Perla M. Dehydration and low temperature separation technologies for liquified natural gas production via electrolysis: a systematic review. J Energy Storage 2020;30:101471. https://doi.org/10.1016/j.est.2020.101471.
[21] Jürgensen L, Ehimen EA, Born J, Holm-Nielsen JB. Dynamic biogas upgrading based on the Sabatier process: thermodynamic and dynamic process simulation. Bioresour Technol 2015;178:323–9. https://doi.org/10.1016/j.biortech.2014.10.069.
[22] Zhang X, Bauer C, Mutel CL, Volkart K. Life Cycle Assessment of Power-to-Gas: approaches, system variations and their environmental implications. Appl Energy 2017;190:326–38. https://doi.org/10.1016/j.apenergy.2016.12.098.
[23] Witte J, Settino J, Biollaz SMA, Schildhauer TJ. Direct catalytic methanation of biogas – Part I: new insights into biomethane production using rate-based modelling and detailed process analysis. Energy Convers Manag 2018;171:750–8. https://doi.org/10.1016/j.enconman.2018.05.056.
[24] Witte J, Kunz A, Biollaz SMA, Schildhauer TJ. Direct catalytic methanation of biogas – Part II: techno-economic process assessment and feasibility reflections. Energy Convers Manag 2018;178:26–43. https://doi.org/10.1016/j.enconman.2018.09.079.
[25] Catarina Faria A, Miguel CV, Madeira LM. Thermodynamic analysis of the CO_2 methanation reaction with in situ water removal for biogas upgrading. J CO_2 Util 2018;26:271–80. https://doi.org/10.1016/j.jcou.2018.05.005.
[26] Bassano C, Deiana P, Lietti L, Visconti CG. P2G movable modular plant operation on synthetic methane production from CO_2 and hydrogen from renewable sources. Fuel 2019;253:1071–9. https://doi.org/10.1016/j.fuel.2019.05.074.
[27] Izzuddin Adnan A, Ong MY, Nomanbhay S, Chew KW, Show PL. Technologies for biogas upgrading to biomethane: a review. Bioeng 2019;6:92. https://doi.org/10.3390/bioengineering6040092.
[28] Zhang X, Witte J, Schildhauer T, Bauer C. Life cycle assessment of power-to-gas with biogas as the carbon source. Sustain Energy Fuels 2020;4:1427–36. https://doi.org/10.1039/C9SE00986H.
[29] Gutierrez-Martín F, Rodríguez-Anton LM, Legrand M. Renewable power-to-gas by direct catalytic methanation of biogas. Renew Energy 2020;162:948–59. https://doi.org/10.1016/j.renene.2020.08.090.

[30] Skorek-Osikowska A. Thermodynamic and environmental study on synthetic natural gas production in power to gas approaches involving biomass gasification and anaerobic digestion. Int J Hydrogen Energy 2022;47:3284–93. https://doi.org/10.1016/j.ijhydene.2021.01.002.

[31] Ghafoori MS, Loubar K, Marin-Gallego M, Tazerout M. Techno-economic and sensitivity analysis of biomethane production via landfill biogas upgrading and power-to-gas technology. Energy 2022;239:122086. https://doi.org/10.1016/j.energy.2021.122086.

[32] Gao J, Liu Q, Gu F, Liu B, Zhong Z, Su F. Recent advances in methanation catalysts for the production of synthetic natural gas. RSC Adv 2015;5:22759–76. https://doi.org/10.1039/C4RA16114A.

[33] Aziz MAA, Jalil AA, Triwahyono S, Ahmada A. CO_2 methanation over heterogeneous catalysts: recent progress and future prospects. Green Chem 2015;17:2647–63. https://doi.org/10.1039/C5GC00119F.

[34] Younas M, Leong LK, Bashir MJK, Nadeem H, Shehzad A, Sethupathi S. Recent advancements, fundamental challenges, and opportunities in catalytic methanation of CO_2. Energy Fuels 2016;30:8815–31. https://doi.org/10.1021/acs.energyfuels.6b01723.

[35] Frontera P, Macario A, Ferraro M, Antonucci P. Supported catalysts for CO_2 methanation: a review. Catalysts 2017;7:59. https://doi.org/10.3390/catal7020059.

[36] Jangam A, Subhasis P, Hongmanorom P, Zhang T, Chen J, Kawi S. A review of recent catalyst advances in CO_2 methanation processes. Catal Today 2020;356:471–89. https://doi.org/10.1016/j.cattod.2020.07.023.

[37] Lee WJ, Li C, Prajitno H, Yoo J, Patel J, Yang Y, Lim S. Recent trend in thermal catalytic low temperature CO_2 methanation: a critical review. Catal Today 2021;368:2–19. https://doi.org/10.1016/j.cattod.2020.02.017.

[38] Hussain I, Jalil AA, Hassan NS, Hamid MYS. Recent advances in catalytic systems for CO_2 conversion to substitute natural gas (SNG): perspective and challenges. J Energy Chem 2021;62:377–407. https://doi.org/10.1016/j.jechem.2021.03.040.

[39] Tsiotsias AI, Charisiou ND, Yentekakis IV, Goula MA. Bimetallic Ni-based catalysts for CO_2 methanation: a review. Nanomaterials 2021;11:28. https://doi.org/10.3390/nano11010028.

[40] Li L, Zeng W, Song M, Wu X, Li G, Hu C. Research progress and reaction mechanism of CO_2 methanation over Ni-based catalysts at low temperature: a review. Catalysts 2022;12:244. https://doi.org/10.3390/catal12020244.

[41] Lach D, Polanski J, Kapkowski M. CO_2 – A crisis or novel functionalization opportunity? Energies 2022;15:1617. https://doi.org/10.3390/en15051617.

[42] Hu F, Ye R, Lu ZH, Zhang R, Feng G. Structure – activity relationship of Ni-based catalysts toward CO_2 methanation: recent advances and future perspectives. Energy Fuels 2022;36:156–69. https://doi.org/10.1021/acs.energyfuels.1c03645.

[43] Tan CH, Nomanbhay S, Shamsuddin AH, Park YK, Hernández-Cocoletzi H, Show PL. Current developments in catalytic methanation of carbon dioxide – A review. Front Energy Res 2022;9:795423. https://doi.org/10.3389/fenrg.2021.795423.

[44] Nieß S, Armbruster U, Dietrich S, Klemm M. Recent advances in catalysis for methanation of CO_2 from biogas. Catalysts 2022;12:374. https://doi.org/10.3390/catal12040374.

[45] Stangeland K, Kalai DY, Li H, Yu Z. Active and stable Ni based catalysts and processes for biogas upgrading: the effect of temperature and initial methane concentration on CO_2 methanation. Appl Energy 2018;227:206–12. https://doi.org/10.1016/j.apenergy.2017.08.080.

[46] Han D, Kim Y, Byun H, Cho W, Baek Y. CO_2 methanation of biogas over 20 wt% Ni-Mg-Al catalyst: on the effect of N_2, CH_4, and O_2 on CO_2 conversion rate. Catalysts 2020;10:1201. https://doi.org/10.3390/catal10101201.

[47] Pastor-Pérez L, Patel V, Le Saché E, Reina TR. CO_2 methanation in the presence of methane: catalysts design and effect of methane concentration in the reaction mixture. J Energy Inst 2020;93:415–24. https://doi.org/10.1016/j.joei.2019.01.015.

[48] Gac W, Zawadzki W, Rotko M, Greluk M, Słowik G, Pennemann H, Neuberg S, Zapf R, Kolb G. Direct conversion of carbon dioxide to methane over ceria- and alumina-supported nickel catalysts for biogas valorization. ChemPlusChem 2021;86:889–903. https://doi.org/10.1002/cplu.202100196.

[49] Mhadmhan S, Ngamcharussrivichai C, Hinchiranan N, Kuchonthara P, Li Y, Wang S, Reubroycharoen P. Direct biogas upgrading *via* CO_2 methanation to high-quality biomethane over NiMg/CNT-SiO_2 fiber catalysts. Fuel 2022;310:122289. https://doi.org/10.1016/j.fuel.2021.122289.

[50] Boggula RR, Fischer H, Casaretto R, Born J. Methanation potential: suitable catalyst and optimized process conditions for upgrading biogas to reach grid requirements. Biomass Bioenergy 2020;133:105447. https://doi.org/10.1016/j.biombioe.2019.105447.

[51] Guilera J, Soto R, Alarcón A, Andreu T. Satisfactory catalyst stability in SNG production using real biogas despite sulfur poisoning evidences at different reactor zones. Fuel 2021;306:121682. https://doi.org/10.1016/j.fuel.2021.121682.

[52] Sanz-Martínez A, Durán P, Mercader VD, Francés E, Peña JÁ, Herguido J. Biogas upgrading by CO_2 methanation with Ni-, Ni–Fe-, and Ru-based catalysts. Catalysts 2022;12:1609. https://doi.org/10.3390/catal12121609.

[53] Chang K, Zhang H, Cheng M-j, Lu Q. Application of ceria in CO_2 conversion catalysis. ACS Catal 2020;10:613–31. https://pubs.acs.org/doi/10.1021/acscatal.9b03935.

[54] Xie Y, Kocaefe D, Chen C, Kocaefe Y. Review of research on template methods in preparation of nanomaterials. J Nanomater 2016;2016:2302595. https://doi.org/10.1155/2016/2302595.

[55] Terribile D, Trovarelli A, Llorca J, de Leitenburg C, Dolcetti G. The synthesis and characterization of mesoporous high-surface area ceria prepared using a hybrid organic/inorganic route. J Catal 1998;178:299–308. https://doi.org/10.1006/jcat.1998.2152.

[56] Atzori L, Cutrufello MG, Meloni D, Cannas C, Gazzoli D, Monaci R, Sini MF, Rombi E. Highly active NiO-CeO_2 catalysts for synthetic natural gas production by CO_2 methanation. Catal Today 2018;299:183–92. https://doi.org/10.1016/j.cattod.2017.05.065.

[57] Klug HP, Alexander LE. X-Ray diffraction procedures. New York: Wiley; 1962.

[58] Rouquerol F, Rouquerol J, Sing KSW, Llewellyn P, Maurin G. Types of adsorption isotherms. In: Adsorption by powders and porous solids: principles, methodology and Applications. 2nd ed. Amsterdam: Academic Press-Elsevier; 2014. p. 12–3.

[59] Atzori L, Rombi E, Meloni D, Sini MF, Monaci R, Cutrufello MG. CO and CO_2 Co-methanation on Ni/CeO_2-ZrO_2 soft-templated catalysts. Catalysts 2019;9:415. https://doi.org/10.3390/catal9050415.

[60] Sagar TV, Sreelatha N, Hanmant G, Surendar M, Lingaiah N, Rama Rao KS, Satyanarayana CVV, Reddy IAK, Sai Prasad PS. Influence of method of preparation on the activity of La-Ni-Ce mixed oxide catalysts for dry reforming of methane. RSC Adv 2014;4:50226–32. https://doi.org/10.1039/C4RA07098D.

[61] Sharma V, Crozier PA, Sharma R, Adams JB. Direct observation of hydrogen spillover in Ni-loaded Pr-doped

ceria. Catal Today 2012;180:2–8. https://doi.org/10.1016/j.cattod.2011.09.009.

[62] Jalowiecki-Duhamel L, Ponchel A, Lamonier C, D'Huysser A, Barbaux Y. Relationship between structure of $CeNi_XO_Y$ mixed oxides and catalytic properties in oxidative dehydrogenation of propane. Langmuir 2011;17:151–1517. https://doi.org/10.1021/la001103y.

[63] Atzori L, Cutrufello MG, Meloni D, Onida B, Gazzoli D, Ardu A, Monaci R, Sini MF, Rombi E. Characterization and catalytic activity of soft-templated NiO-CeO_2 mixed oxides for CO and CO_2 co-methanation. Front Chem Sci Eng 2021;15:251–68. https://doi.org/10.1007/s11705-020-1951-8.

[64] Liu Z, Chu B, Zhai X, Jin Y, Cheng Y. Total methanation of syngas to synthetic natural gas over Ni catalyst in a micro-channel reactor. Fuel 2012;95:599–605. https://doi.org/10.1016/j.fuel.2011.12.045.

[65] Gao J, Wang Y, Ping Y, Hu D, Xu G, Gu F, Su F. A thermodynamic analysis of methanation reactions of carbon oxides for the production of synthetic natural gas. RSC Adv 2012;2:2358–68. https://doi.org/10.1039/c2ra00632d.

[66] Aldana PAU, Ocampo F, Kobl K, Louis B, Thibault-Starzyk F, Daturi M, Bazin P, Thomas S, Roger AC. Catalytic CO_2 valorization into CH_4 on Ni-based ceria-zirconia. Reaction mechanism by operando IR spectroscopy. Catal Today 2013;215:201–7. https://doi.org/10.1016/j.cattod.2013.02.019.

[67] Berlouis LEA, Jubin C, McMillian BG, Morrow J, Spicer MD, Tang LP, Bordelanne O, Weston M. Enhanced hydrogen storage in Ni/Ce composite oxides. Phys Chem Chem Phys 2007;9:6032. https://doi.org/10.1039/B710026D. 3039.

[68] Onrubia-Calvo JA, Quindimil A, Davo-Quiñonero A, Bermejo-Lopez A, Bailon-Garcia E, Pereda-Ayo B, Lozano-Castello D, Gonzalez-Marcos JA, Bueno-Lopez A, Gonzalez-Velasco JR. Kinetics, model discrimination, and parameters estimation of CO_2 methanation on highly active Ni/CeO_2 catalyst. Ind Eng Chem Res 2022;61:10419–35. https://doi.org/10.1021/acs.iecr.2c00164.

[69] Italian Ministry of Economic Development DM. 18/05/2018 – regola tecnica sulle caratteristiche chimico fisiche e sulla presenza di altri componenti nel gas combustibile. 2018. https://www.mise.gov.it/index.php/it/normativa/decreti-ministeriali/decreto-ministeriale-18-maggio-2018-gas-combustibile-aggiornamento-regola-tecnica.

[70] Moioli E, Mutschler R, Borsay A, Calizzi M, Züttel A. Synthesis of grid compliant substitute natural gas from a representative biogas mixture in a hybrid Ni/Ru catalysed reactor. Chem Eng Sci X 2020;8:100078. https://doi.org/10.1016/j.cesx.2020.100078.

[71] European Committee for standardization CEN/TC 234. EN 16726 gas infrastructure – quality of gas – group H infrastructure. 2015. p. 49.

[72] K. Altfeld, D. Pinchbeck, Admissible hydrogen concentrations in natural gas systems, Reprint: gas for energy 03/2013, ISSN 2192-158X, DIV Deutscher Industrieverlag GmbH, https://www.gerg.eu/wp-content/uploads/2019/10/HIPS_Final-Report.pdf.

[73] Dvgw G. 262 – use of gas for renewable resources in public gas supply. 2011.

[74] Villante C, Genovese A. Hydromethane: a bridge towards the hydrogen economy or an unsustainable promise? Int J Hydrogen Energy 2012;37:11541–8. https://doi.org/10.1016/j.ijhydene.2012.03.066.

[75] National Renewable Energy Laboratory. Blending hydrogen into natural gas pipelines networks: a review of key issues". Denver. 2013. https://www.nrel.gov/docs/fy13osti/51995.pdf.

[76] Guandalini G, Campanari S, Romano MC. Power-to-gas plants and gas turbines for improved wind energy dispatchability: energy and economic assessment. Appl Energy 2015;147:117–30. https://doi.org/10.1016/j.apenergy.2015.02.055.

[77] Korb B, Kawauchi S, Wachtmeister G. Influence of hydrogen addition on the operating range, emissions and efficiency in lean burn natural gas engines at high specific loads. Fuel 2016;164:410–8. https://doi.org/10.1016/j.fuel.2015.09.080.

[78] Pellegrino S, Lanzini A, Leone P. Greening the gas network – the need for modelling the distributed injection of alternative fuels. Renew Sustain Energy Rev 2017;70:266–86. https://doi.org/10.1016/j.rser.2016.11.243.